Quantification of corrosion-like defect in pipelines using multi-frequency identification of non-dispersive torsional guided waves

Citation for published version:
Zhu, C, Xu, ZD, Zang, X, Xu, Y, Miao, C & Lu, Y 2024, 'Quantification of corrosion-like defect in pipelines using multi-frequency identification of non-dispersive torsional guided waves', *Journal of Engineering Mechanics*, vol. 150, no. 8, 04024050, pp. 1-12. https://doi.org/10.1061/JENMDT.EMENG-7587

Digital Object Identifier (DOI):
10.1061/JENMDT.EMENG-7587

Published In:
Journal of Engineering Mechanics

Quantification of corrosion-like defect in pipelines using multi-frequency identification of non-dispersive torsional guided waves

Chen Zhu [1], Zhao-Dong Xu, A. M. ASCE [2*], Xulei Zang [3], Yan-Wei Xu [4], Changqing Miao [5], Yong Lu, F. ASCE [6].

Abstract

Pipeline guided wave inspection is an efficient tool for determining a defect location. However, quantifying the defect size remains a challenging task. This paper proposes a quantification method for corrosion-like defects in pipelines based on the multi-frequency identification of non-dispersive torsional guided waves. Firstly, a theoretical scattering model describing the T(0,1) wave's interaction with simplified corrosion-like damage is introduced. Subsequently, a multi-frequency identification method is proposed, enabling the inverse quantification of defect parameters by a defined spectral defect index (SDI). To implement this approach, a pseudo pulse-echo configuration is devised, which contains two rings of piezoelectric transducers attached on the pipeline's out surface. Finite element (FE) models are employed to test the performance of the proposed method for both axisymmetric and non-axisymmetric defects, and an analysis of the robustness of the method is also conducted. The

---

[1] Ph.D. Candidate, China-Pakistan Belt and Road Joint Laboratory on Smart Disaster Prevention of Major Infrastructures, Southeast University, 211189, Nanjing, China E-mail: zhchen_cz@163.com
[2] Professor, China-Pakistan Belt and Road Joint Laboratory on Smart Disaster Prevention of Major Infrastructures, Southeast University, 211189, Nanjing, China (corresponding author). E-mail: zhdxu@163.com
[3] Ph.D. Candidate, China-Pakistan Belt and Road Joint Laboratory on Smart Disaster Prevention of Major Infrastructures, Southeast University, 211189, Nanjing, China. E-mail: zxlseu@seu.edu.cn
[4] Lecture. School of Civil Engineering and Communication, North China University of Water Resources and Electric Power, 450045, Zhengzhou, China. E-mail: xuyanwei_v587@163.com
[5] Professor, China-Pakistan Belt and Road Joint Laboratory on Smart Disaster Prevention of Major Infrastructures, Southeast University, 211189, Nanjing, China. E-mail: chqmiao@seu.edu.cn
[6] Professor, Institute for Infrastructure and Environment, School of Engineering, The University of Edinburgh, Edinburgh EH9 3 JL, UK. E-mail: yong.lu@ed.ac.uk

results show that this method has good accuracy even for signals with a very low signal to noise (SNR) ratio. Furthermore, a FE model is developed to validate the feasibility of this method for long-distance detection considering attenuation effect. Finally, experimental validation of the proposed method demonstrates close agreement between predicted and actual defect sizes, showing its potential for practical applications.

Keywords

Ultrasonic guided wave; Defect quantification; Multi-frequency identification; Reciprocity theorem; Spectral defect index.

Introduction

Pipeline systems are widely used in transportation of petrochemical products (Lu et al. 2023)(Peng et al. 2023). However, due to the harsh working conditions, corrosion frequently occurs and affects the pipeline integrity (Xu et al. 2021). Guided wave detection technology is an efficient tool for non-destructive testing (NDT) (Zhang et al. 2022)(Zhang et al. 2023)(Wang et al. 2023) and structural-health monitoring (SHM) (Croxford et al. 2007)(Liu et al. 2021). For pipeline defect detection, transducers are usually attached equally around the circumference on the pipe surface to generate axisymmetric plane guided waves. Since the plane guided wave does not have beam divergence (Chua et al. 2019), a long range (over 10 m) inspection effect can be achieved at relatively low frequencies. As such , pipeline guided wave inspection usually serves as a screening tool for defect localization (Zang et al. 2023), while the distance-amplitude correction (DAC) lines is applied to assess the severity of defect qualitatively (Catton et al. 2008). However, more precise quantification of defect is still a challenging task in a guided wave detection approach (Mitra and Gopalakrishnan 2016).

The scattering model describes the interaction of fundamental guided wave with various types of defects, and it is a basis for defect quantification. In order to examine the theoretical basis of pipeline guided wave scattering, Ditri (Ditri 1994) developed a theoretical model to describe the pipeline guided wave scattering by circumferential cracks with S-parameter formalism. Lee et al. (Lee et al. 2018) employed a wave field superposition technique along with the reciprocity theorem to simplify the solution of the T(0,1) scattering problem.

In order to reveal characteristics of the guided wave when interacting with more complex defects, finite element (FE) simulation has been carried out. Demma et al. (Demma et al. 2004) employed FE simulation to study the interaction of guided waves with rectangular notch defect in pipelines, and summarized the effects of pipe size, defect size, guided-wave mode, and frequency on reflection from the notches. Carandente et al. (Carandente and Cawley 2012) further studied the reflection of T(0,1) mode with a simulated tapered step notch. They analyzed the effects of different contours and depths on the reflection coefficients, and argued that the corresponding findings could be used to evaluate the defect depth according to the defect circumferential range and the maximum reflection coefficient. Lovstad and Cawley (Løvstad and Cawley 2011) analyzed the effect of circular holes on T(0,1) reflection and proposed a relationship between pit cluster shape and the reflection coefficient. Zhu et al. (Zhu et al. 2022) studied the interaction between L(0,2), T(0,1) wave with dent defect, and demonstrated the difference in the scattering mechanisms as compared with notch defect. Considering the fact that using finite element modelling is relatively time-consuming to obtain a complete solution, Duan and Kirby (Duan and Kirby 2015) introduced a semi-analytical method to solve the guided wave scattering problem. They introduced a weighted residual formulation based on the Galerkin's principle to account for arbitrarily shaped defects in pipelines. The method was shown to be a highly efficient numerical approach.

Based on the scattering features from defects, several signal processing methods have been proposed to decompose the reflected wave and quantify defects. Wang et al. (Wang et al. 2010) used the Hilbert–Huang transform to decompose the reflection signals from front and rear edges of the defect, so the axial length of the defect can be obtained. Tse and Wang (Tse and Wang 2013) proposed an optimized matching pursuit (MP) method by analyzing the interference between the reflection components, which can extract axial length information by separated reflection signal. However, such methods are mainly applied in axisymmetric defects.

Some researchers have found that there exists a certain relationship between scattering amplitude and the wavelength-to-defect length ratio in various types of defects, such as notch (Demma et al. 2004), hole (Løvstad and Cawley 2011) and dent (Zhu et al. 2022). Therefore, there is a potential solution that utilizes the relationship between the amplitude and the wavelength-to-defect length ratio parameter to quantify defect, and this has attracted much research interest recently. Wang et al. (Wang et al. 2019) used lamb wave inspection at multiple frequencies, and the method was shown to improve the probability of detection as compared with single-frequency excitation. Xu et al.(Xu et al. 2023) used frequency-dependent scattering of wide band laser-generated Rayleigh waves to characterize vertical surface crack. Shan et al.(Shan et al. 2022) proposed a defect quantification algorithm based on the wave reflections from the defect and wave-guided end, and used it to quantify geometric parameters of the defects in cylindrical structures. Generally speaking, these methods are in the initial phase of development, and the corresponding research and exploration of potential applications are still insufficient.

This paper proposes a multi-frequency identification approach for quantifying pipeline defect using a scattering model between T(0,1) waves and corrosion-like defects. The organization of the paper is as follows. Firstly (Section 2), a scattering model is introduced, which describes the scattering wave from a T(0,1) wave interacting with simplified corrosion-like defect in pipeline. In Section 3, a methodology for inversely quantifying the defect by a multi-frequency method is proposed, and a corresponding inspection configuration is designed. In Section 4, the proposed method is validated by FE simulation, and the robustness is also tested. An experimental validation is presented in Section 5. Finally, Section 6 summarizes the main conclusions.

Basic theory

Characterization of T (0,1) mode

For the guided wave propagation in an elastic isotropic hollow cylinder, three types of wave modes are mainly studied, namely, longitudinal mode, torsional mode, and flexural mode. The particle displacements can be described as (Rose 2014):

$$u_r(r,z,t) = U_r(r)\cos(m\theta)\, e^{i(kz-\omega t)}, \tag{1a}$$

$$u_\theta(r,z,t) = U_\theta(r)\sin(m\theta)\, e^{i(kz-\omega t)}, \tag{1b}$$

$$u_z(r,z,t) = U_z(r)\cos(m\theta)\, e^{i(kz-\omega t)}. \tag{1c}$$

where, $U_r(r)$, $U_\theta(r)$, $U_z(r)$ are the displacement profiles of radial displacement, tangential displacement, and axial displacement in the radial direction, respectively. r and z denote radial and axial locations respectively. m is the circumferential order of a wave mode. k, ω and t denote wave number, angular frequency and time respectively.

T(0,1) mode offers several advantages, such as nondispersive and no leakage to the surrounding fluid, making it particularly attractive for long-range inspection (Niu et al. 2019)(Alleyne et al. 2009). For this reason, only T(0,1) mode is considered here, and the wave displacement can be simplified to only include the tangential displacement shown in Eq. (1b).

The tangential displacement equation of motion is:

$$\frac{d^2U_\theta}{dr^2}+\frac{1}{r}\frac{dU_\theta}{dr}+\left[\left(\frac{\omega^2}{c_T^2}-k^2\right)-\frac{1}{r^2}\right]U_\theta=0 \quad (2)$$

For the zero mode torsional wave, $\frac{\omega^2}{c_T^2}-k^2=0$. Therefore, $U_\theta(r)$ can be expressed as $U_\theta(r)=Ar$, with A being the wave amplitude.

Consider an incident T(0,1) wave propagation forward in a pipe. The incident wave can be described as:

$$u_\theta^{in}(z,t)=A^{in}U_\theta(r)e^{i(kz-\omega t)}, \quad (3a)$$

$$\tau_{z\theta}^{in}(z,t)=ik\mu u_\theta^{in}(z,t). \quad (3b)$$

where, the superscript "in" indicates incident wave.

Scattering model

In this paper, we adopt the elastodynamic reciprocity theorem (Balogun and Achenbach 2020)(Pau et al. 2016) to model the scattering wave from a simplified corrosion-like defect as shown in Fig. **1**. The scattered torsional wave is the response due to the shear stress on the defect introduced by the incident T(0,1) wave. Since the two surfaces of defect are simplified as parallel to radial direction, only the shear stress $\tau_{z\theta}$ on the defect surface is considered. The forward scattered torsional wave generated by the rear surface can be described as:

$$u_{\theta}^{sc+}(z,t) = A^{sc+}U_{\theta}(r)e^{ikz}, \tag{4a}$$

$$\tau_{z\theta}^{sc^+}(z,t) = i\mu k A^{sc+}U_{\theta}(r)e^{ikz}. \tag{4b}$$

The backward scattered torsional wave generated by the front surface can be described as:

$$u_{\theta}^{sc^-}(z,t) = A^{sc-}U_{\theta}(r)e^{-ikz}, \tag{5a}$$

$$\tau_{z\theta}^{sc^-}(z,t) = -i\mu k A^{sc-}U_{\theta}(r)e^{-ikz}. \tag{5b}$$

where, A^{sc+} and A^{sc-} represents amplitude of the forward and backward scattered wave, respectively.

The elastodynamic reciprocity theorem establishes a connection between two distinct elastodynamic states within the same body *V* and its corresponding surface *S* (Phan et al. 2013). Since no body force is assumed to exist in each state (Kubrusly and Dixon 2021)(Pau et al. 2015), it provides:

$$\iint_{S} \left(\tau_{ij}^{B}u_{j}^{A} - \tau_{ij}^{A}u_{j}^{B}\right)n_{i}ds = 0 \tag{6}$$

where, τ_{ij} and u_i denote stress and displacement, respectively. n_i is the unit outward normal to the surface S. The superscripts A and B denote two elastodynamic states. In this case, state A corresponds the scattering of T(0,1) wave generated by defect and propagating in both forward and backward directions. State B denotes a virtual incident T(0,1) wave propagating in the forward direction without defect, as (Lee et al. 2018):

$$u_{\theta}^{vi}(z,t) = A^{vi}U_{\theta}(r)e^{ikz}, \tag{7a}$$

$$\tau_{z\theta}^{vi}(z,t) = i\mu k A^{vi}U_{\theta}(r)e^{ikz}. \tag{7b}$$

where, the subscript vi indicates virtual incident wave.

The contour S can be decomposed to the S_1 , S_2… S_8 as shown in Fig. **2**. The integration on each surface is called J_1 , J_2… J_8, respectively. The integrations on the upper and bottom surfaces are zero since the $\tau_{z\theta}$ is zero on these boundary free surfaces, yielding $J_2 = J_4 = J_6 = J_8 = 0$. The integrations on S_3 is zero since the forward scattered wave and incident wave are in the same direction on state A and B. Therefore, the integrations can be reduced to:

$$\iint_S (\tau_{ij}^B u_j^A - \tau_{ij}^A u_j^B)\, n_i ds = J_1 + J_5 + J_7 = 0 \tag{8}$$

For J_1, J_5 and J_7 substitution of Eqs. (4), (5) and (7) to Eq. (6), and integrating over *r* from a to *b* and over θ from 0 to 2π yields:

$$J_1 = \int_a^b (\tau_{z\theta}^{vi} u_\theta^{sc-} - \tau_{z\theta}^{sc-} u_\theta^{vi}) * (-1) r dr = 4i\pi\mu k A^{vi} A^{sc-} \int_a^b {U_\theta}^2(r) r dr \tag{9}$$

The shear stress generated by incident torsional wave can be considered as uniform due to the small ratio of defect depth to incident wavelength. The generated shear stress can be described as:

$$\tau'_{z\theta} = i\mu k A^{in} U_\theta(r) e^{ikz} \tag{10}$$

and the displacement generated by the $\tau'_{z\theta}$ is u'_θ.

For the integrations on the defect surfaces:

$$J_5 = 2\pi \int_a^b (\tau_{z\theta}^{vi} u_\theta'^{+} - \tau_{z\theta}'^{+} u_\theta^{vi}) * (-1) r dr, \tag{11}$$

$$J_7 = 2\pi \int_a^b (\tau_{z\theta}^{vi} u_\theta'^{-} - \tau_{z\theta}'^{-} u_\theta^{vi}) r dr. \tag{12}$$

Since the displacements are opposite and shear stresses are the same on the two surfaces of the defect in state A, it yields:

$$J_5 + J_7 = -2\pi \int_{b-d}^b \tau_{z\theta}^{vi} (u_\theta'^{+} - u_\theta'^{-}) dr \tag{13}$$

Since u_θ^{sc+} and u_θ^{sc-} are generated by $\tau_{z\theta}^{in}$ on the defect surface, the displacement can be approximated as:

$$u'^{\pm}_{\theta} = u^{in}_{z\theta} e^{\pm ikle/2}, \tag{14}$$

therefore:

$$\begin{aligned} J_5 + J_7 &= -\int_{b-d}^{b} \tau^{vi}_{z\theta} u^{in}_{z\theta} \left(e^{\frac{ikle}{2}} - e^{-\frac{ikle}{2}}\right) dr \\ &= 4i\pi\mu k A^{vi} A^{in} sin(kle) \int_{b-d}^{b} {U_\theta}^2(r) r dr. \end{aligned} \tag{15}$$

Substitution of Eqs. (9) and (15) to Eq. (8) yields:

$$\left|\frac{A^{sc}}{A^{in}}\right| = \sin(kL_e)\frac{b^4 - (b-d)^4}{b^4 - a^4}, \tag{16}$$

where d is the depth of wall-thinning defect.

Scheme of multi-frequency identification method

Method

Section 2 has introduced the theoretical model describing a scattering model for a wall-thinning defect. The quantification of the defect severity is an inverse problem (Liu et al. 2023) (Gao et al. 2024). For this purpose, we introduce a spectral defect index (SDI), which measures the scattering amplitude in the frequency domain. The frequency dependent index SDI is subsequently compared with the SDI calculated by the theoretical model, and the severity of the defect can be estimated by minimizing the difference between the measured and theoretical SDI results.

For the sake of enhancing the precision and robustness in the defect quantification, it is necessary to obtain more SDI values across varying frequencies. Therefore, we propose a multi-frequency identification (MFI) method that provides more information related to the size of defect. We use two different approaches to get the SDI values as follows. 1) Single excitation: here a pulse signal is excited at one central frequency which is below the cut-off frequency of T(0,2), and the SDI is calculated at 3 dB bandwidth of the central frequency. 2) Multiple excitation: here different pulse signals are excited within the frequency range below the cut-off frequency of T(0,2) separately, and the SDI is calculated at the central frequencies of each pulse signal. The performance of these two approaches will be compared in the following test.

Fig. **3** shows a schematic of the MFI method. First we measure the SDIs at a frequency range which is below the T(0,2) cutoff frequency. The excited signal from the transducers and reflected signal from the defect are measured separately. Then, the spectral defect index is calculated as:

$$\mathrm{SDI}(f) = \frac{S^s(f)}{S^i(f)}, \tag{17}$$

where, $S^s(f)$ and $S^i(f)$ are the spectral responses of the scattering wave and incident wave calculated by fast Fourier transform (FFT), respectively.

In order to quantify the defect, the SDIs are compared with the results calculated from the theoretical model. Eq. (18) is used to calculate the difference between the measured results and theoretical results in terms of root mean square error (RMSE):

$$RMSE(d,l) = \sqrt{\frac{1}{n}\sum_{i=1}^{n}\left(SDI_m(f_i) - SDI_t(f_i)|_{d,l}\right)^2}, \tag{18}$$

where *n* is the number of SDI, $\mathrm{SDI}_m(f_i)$ is the measured SDI at frequency f_i, and $\mathrm{SDI}_t(f_i)|_{d,l}$ is the theoretical SDI at frequency f_i with a defect of depth d and length l. The RMSE is used to compare the difference between the measured defect SDI and the theoretically calculated defect SDI of depth *d* and length *l*. The defect sizes *d* and *l* are selected within a certain possible range, and the maximum $\mathrm{RMSE}_{\max}$ and the minimum $\mathrm{RMSE}_{\min}$ within this range can be obtained. In order to determine the sizes of the defect, a nominal probability function is proposed as,

$$P(d,l) = \frac{(1/\mathrm{RMSE}(d,l) - 1/\mathrm{RMSE}_{max})}{(1/\mathrm{RMSE}_{min} - 1/\mathrm{RMSE}_{max})}. \quad (19)$$

Where $P(d,l)$ denotes the possibility that the measured defect depth is d and the length is l. If $P(d,l)$ is close to 1, it means that the RMSE for defect with depth d and length l is close to the minimum RMSE calculated in the possible size range, indicating a high probability of defect to be of that size. Conversely, if $P(d,l)$ is close to 0, indicating that the measured defect is least likely to be of that size. Using Eq. (19), we can plot a probability map to predict the defect sizes.

Inspection configuration

In the traditional pulse-echo method, the transducer acts as both the exciter and the sensor. However, the incident wave signal is difficult to obtain, and the SDI of the defect cannot be directly measured. To deal with this problem, in this paper we propose a pseudo pulse-echo method that requires two rings of transducers. One ring is used for T(0,1) wave generation, and another ring is used for measuring the incident wave and reflection wave from defect, as shown in Fig. **4**. The whole process of the inspection can be described by Eqs. (20), (21) below:

$$T(f) = F(V_{in}(t)) \cdot E(f) \cdot e^{-\alpha z_1} \cdot R(f), \quad (20)$$

where $T(f)$ is the transmission wave measured by the transducer ring 2 in frequency domain, $F(\,)$ is Fourier transform function, $V_{in}(t)$ is the input signal in time domain, $E(f)$ is frequency response of transducer ring 1 for T(0,1) wave excitation, and $R(f)$ is frequency response of transducer ring 2 for T(0,1) wave reception.

$$S(f) = F(V_{in}(t)) \cdot E(f) \cdot e^{-\alpha z_1} e^{-2\alpha z_2} \cdot \mathrm{SDI}(f) \cdot R(f), \quad (21)$$

where $S(f)$ is the scattered wave measured by the transducer ring 2 in frequency domain, α is the attenuation coefficient for T(0,1) wave propagating in the pipe.

Eq. (21) represents the frequency response function of the T(0,1) wave throughout the entire detection process. It describes the process in which (i) the T(0,1) wave is firstly excited by ring 1, $E(f)$, through the input signal $V_{in}(f)$, (ii) it then propagates to the defect considering attenuation $e^{-\alpha(z_1+z_2)}$, (iii) the interaction between incident T(0,1) wave and the defect, denoted as $\mathrm{SDI}(f)$, (iv) the reflected wave considering attenuation $e^{-\alpha z_2}$, and finally (v) measured by the ring 2 by $R(f)$.

The SDI can be obtained by dividing Eq. (21) by Eq. (20), as:

$$\mathrm{SDI}(f) = \frac{S(f)e^{2\alpha(f)z_2}}{T(f)}. \tag{22}$$

If $\alpha(f)$ has no significant change in the frequency range, and z_2 is not very long, the attenuation term $e^{2\alpha(f)z_2}$ can be ignored. Otherwise, the attenuation needs to be considered, and the effect of attenuation to the quantification accuracy will be discussed in Section 4.4.

In the following sections, we will realize the proposed method through FE simulation and laboratory experiment.

FE validation

FE set-up

To validate the proposed method, a three-dimensional FE simulation is carried out using commercial FE analysis software, ABAQUS/Explicit 6.14-3. Fig. 5 shows the configuration of the FE model setup. The pipe is made of aluminum, which has Young's modulus $E = 69.0$ GPa, Poisson's ratio $\upsilon = 0.33$ and density $\rho = 2700$ kg m^{-3}. The pipe has a length of 600 mm, an outer diameter of 90 mm, and a wall thickness of 3 mm. In the FE model, the pipe is modeled using C3D8R elements. To ensure the accuracy of the simulation results, the size of elements is 1 mm which is less than 1/20 the shortest wavelength, and the analysis time step is 0.1 μs which is less than $1/(20f_c)$, with f_c being central frequency of the applied pulse signal. The excitation signal is a 5-cycle Hanning window-modulated sinusoid tone-burst, and it is imposed by applying tangential displacement around the outer circumference at the pipe end to generate T(0,1) mode. The reflection signals are measured by a circle of 16 points at a distance of 200 mm from the excitation end in a typical way (Xu et al. 2019).

FE realization

Axisymmetric defect

An axisymmetric defect scenario is firstly simulated. The defect is simulated by a reduction of the thickness throughout 1 mm, over a length of 30 mm at a distance of 400 mm from the excitation end, as indicated in Fig. **5**.

For the single-excitation method, a central frequency of 100 kHz is selected for the excitation pulse signal, while for the multiple-excitation method a frequency range from 50 kHz to 150 kHz with 10 kHz step is selected. The incident wave and reflected wave are measured at this frequency range as can be seen in Fig. **6**.

The SDI are calculated by dividing the incident wave amplitude to the reflection wave amplitude in frequency domain, and the results are shown in Fig. **7** (a) for single-excitation method and Fig. **8** (a) for multiple-excitation method. By calculating the RMSE between the calculated SDI with the theoretical model, the probability map of defect size can be obtained as can be seen in Fig. **7** (b) for single-excitation method and Fig. **8** (b) for multiple-excitation method. The defect sizes of maximum probability are 1.02 mm in depth and 30.6 mm in length for the single excitation, and 1.11 mm in depth and 30.3 mm in length for the multiple-excitation method. Both sets of the results are very close to the actual defect sizes that are set in the FE model.

Non-axisymmetric defect

Non-axisymmetric defects are more common in pipeline. For the non-axisymmetric cases, Eq. (16) should be modified as:

$$\left|\frac{A^{sc}}{A^{in}}\right| = sin(kL_e)\frac{b^4-(b-D)^4}{b^4-\alpha^4}\frac{\theta_d}{2\pi}, \tag{23}$$

where θ_d is the circumferential degree which can be seen in Fig. **5**.

Based on Eq. (23) the amplitude of the SDI is linear to the circumferential degree, which means if an unknown defect was considered as an axisymmetric case, the axial length of defect could still be quantified accurately, but the depth would be underestimated. In fact, the circumferential extent of the defect may be judged by using mode conversion ratio (Zhu et al. 2022). Since the circumferential degree is not the main focus in this paper, we assume that the circumferential extent is a known parameter. In the FE simulation we created two non-axisymmetric models with defect of 1 mm in depth and 30 mm in axial length, while the circumferential extent is set at $\pi/2$.

The defects are quantified as 1.12 mm in depth and 30.3 mm in axial length using the multiple excitation method as can be seen in Fig. **9** (a). The results are quite accurate comparing to the actual defect in the FE models, demonstrating the feasibility to be applied in a non-axisymmetric defect situation. Even if the circumferential extent parameter is not known and the defect is treated as an axisymmetric case, the depth of the defect is underestimated while the axial length of defect can still be quantified as the same, as can be seen in Fig. **9** (b).

Robustness testing

The axisymmetric defect case with 1-mm depth and 30-mm length is used to test the robustness of the proposed multi-frequency method. To simulate a real inspection situation, Gaussian white noise is added to the FE simulation results. The signal-to-noise ratio (SNR) ranges from 5 dB to 30 dB.

Fig. 10 (a) shows the received signal with 10 dB SNR as an example. Fig. 10 (b) shows the variation of the percentage error in the predicted defect size with the SNR. It can be observed that even for the 5-dB SNR case, the percentage errors of depth and length are just between -10% to 20%, which may be regarded as acceptable. For cases with SNR over 10 dB, the percentage errors for single excitation are only between -5% to 5%. The percentage error for the depth prediction using multiple excitation detection is around 10%, which is slightly higher than other results. In general, both the single excitation method and the multiple excitation method exhibit high accuracy and strong robustness. In terms of predicting defect depth, the single excitation method demonstrates greater accuracy.

Attenuation effect

In order to demonstrate that the proposed method can be applied under long-distance and attenuation conditions, the distance between the defect and the sensor is set to be 10 m, and the Rayleigh damping model is introduced to simulate attenuation effect in FE model. The damping ratio ζ is defined as:

$$\zeta = \frac{1}{2}\left(\frac{\alpha}{\omega_n} + \beta\omega_n\right), \quad (24)$$

where, ω_n is the natural frequency. α and β are two parameters of the damping model, where $\alpha = 5$ and $\beta = 0$ are set to simulate the attenuation in pipeline guided wave propagation (Mei and Giurgiutiu

2019). Fig. 11 shows the time-domain signals and corresponding Hilbert envelopes collected by nodes located at distances of $d_1 = 0.5\ m$ and $d_2 = 2.5\ m$ from the excitation nodes. The attenuation coefficient $\alpha(f)$ is calculated by Eq. (25) at each central frequency.

$$\alpha(f) = \frac{-20\log_{10}(A_2/A_1)}{d_2 - d_1}, \tag{25}$$

where, A_1 and A_2 are the peak amplitudes of the Hilbert envelopes of the time-domain signals collected at $d_1 = 0.5\ m$ and $d_2 = 2.5\ m$ respectively. Fig. 12 shows the attenuation coefficients at different frequencies, where the tendency is similar with the theoretical results (Marzani 2008). It can be seen that as the frequency increases, the amplitude and change of attenuation coefficients increase.

In the present example, the single-excitation method at 50, 100, 150 kHz and the multi-excitation method with 50-150 kHz central frequencies are all used for the defect quantification, the results are shown in Table **1**. It can be observed that attenuation has a certain impact on quantification accuracy. For the single-excitation method, the quantification accuracy decreases as the center frequency increases. For the multi-excitation method, the quantization accuracy is also reduced since the attenuation coefficient changes significantly in the 100-150 kHz range. These results show that, if a relatively low frequency (< 100 kHz in this case) is used, the proposed method maintains satisfactory accuracy in long-distance detection considering attenuation effect.

Experimental validation

Experimental set-up

In order to validate the proposed method for pipeline defect quantification in a physical environment, a series of laboratory experiments have been conducted on an aluminum pipe (Al-6061).

The pipe has the same dimensions as used in the FE simulation, and two transducer rings are used to excite and receive T(0,1) guided wave respectively. As seen from the experimental setup in Fig. **13**, each transducer ring contains 16 rectangle PZT strip transducers, which are equally bonded along the pipe's circumferential direction, for T(0,1) wave generation and reception. The distance between the excitation ring and reception ring is 200 mm along the axial direction of the pipe. PZT transducers are type PZT-5H ceramic with length 8 mm, width 4 mm, and thickness 1 mm. These PZT transducers are mounted on the surface of the pipe using epoxy.

The defect is made as axisymmetric wall-thinning defect with 40-mm axial length and 1-mm depth, located at 400 mm away from the excitation end, and it is created by a computer numerical control (CNC) cutting machine to ensure the accuracy of the defect sizes.

The piezoelectric wafers are driven by a five-cycle Hanning window-modulated sinusoidal tone-burst signal generated by an arbitrary function generator (Tektronix AFG3022) and amplified by a high-voltage power amplifier (Pintech HA-205). The transmission and reflection signals were measured by the ring of piezoelectric sensors and superimposed collected using a digital oscilloscope (Rohde & Schwarz, RTB-2002).

Experimental realization

Fig. **14** (a), (b) show the time domain signal for 50 and 150 kHz excitation, respectively. It can be seen that the transmission wave is the first wavepacket and reflection wave from defect is the second wave packet in the time domain and easy to extract. These signals are then calculated in the frequency domain, and subsequently the SDI can be obtained. Fig. **15** (a), **16** (a) and **17** (a) show the results for single excitation at 50, 100, 150 kHz , and the results for multiple excitation method are shown in Fig. **18** (a). The dashed line is the best fitted theoretical model. By comparing the RMSE between the experimental and theoretical results with different sizes, we can draw the probability map to predict the defect sizes, as shown in Fig. **14** (b), **16** (b) and **17** (b) for single excitation at 50, 100, 150 kHz and Fig. **18** (b) for the multiple excitation method.

In order to avoid false predictions in using the multiple excitation method, an additional parameter, i.e. the number of peaks of SDI curve, can be utilized to narrow the possible axial length range firstly. There are three peaks in the measured SDI curve from 50 kHz to 150 kHz as can be seen in Fig. **18** (a), and according to the theoretical model, the axial length should be between 370 and 470 mm. Then, the probability map is narrowed as can be seen from a red frame in Fig **18** (b) to avoid false predictions.

The calculated defect results are summarized in Table **2** and **3**. The percentage errors for axial length prediction is around 7% except for the 150 kHz cases. Excluding a false prediction in the 150 kHz case, the percentage error from the other prediction result is around 5%. The percentage errors for the depth prediction are around 30%. In other words, for the actual defect of 1-mm depth and 40-mm axial length, the predicted defect length is around 42.5 mm, and the predicted defect depth is around 1.35 mm. These results demonstrate that the proposed method maintains satisfactory accuracy in a physical laboratory testing environment.

The percentage errors for the defect depth are higher than those for the axial length, which is understandable and maybe attributed primarily to two reasons: 1) The axial length of the defect is significantly larger than its depth in terms of the absolute dimension, thus for the same magnitude of error in sizes, the percentage error in depth is obviously larger. 2) As the scattering amplitude directly influences the predicted depth value without directly affecting the predicted length value, there are more factors influencing the depth prediction in practical detection. The results also show the effect of central frequency on the predicted defect parameters, and this is more evident in the depth prediction. The percentage errors are 40% and 22% corresponding to the central frequency of 50 kHz and 150 kHz, respectively. This trend suggests that a higher central frequency can effectively improve the prediction accuracy, especially for the depth prediction.

Conclusions

This paper proposes a new approach for pipeline defect quantification based on T(0,1) guided wave. A forward theoretical model describing the interaction between T(0,1) wave with wall-thinning defect is introduced, and an inverse quantification process is realized by the proposed multi-frequency identification method.

The theoretical scattering model, which is based on the reciprocity theorem, considers the T(0,1) wave interaction with a wall-thinning defect in that the scattering amplitude is a superposition of the front and back edges of the defect. Thus, the defect depth and axial length are represented, and their effect on the model is expressed as frequency dependent amplitudes. On this basis, a spectral defect index (SDI) is introduced which is associated with defect sizes and therefore allows quantifying the defect through an inverse procedure. An inspection configuration is proposed to actually measure SDI. Two specific methods for obtaining SDI are proposed, one using a single excitation method and another using a multiple excitation method.

Finite element models are employed to test the performance and robustness of the proposed method. Both axisymmetric and non-axisymmetric defect cases are considered. The predicted results from the FE simulation show excellent accuracy, with a percentage error below 10% for the depth prediction and below 2% for the axial length prediction. The robustness of the technique is tested by adding Gaussian white noise to the received signals. The results show that for 5-dB SNR, the percentage error for depth prediction is between -10% to 20%, and for axial length is between -5% to 10%. For 10-30 dB SNR cases, the percentage errors are generally between -5% to 10%, showing its strong robustness to noise disturbance. In addition, a FE model for long-distance detection considering attenuation effect is employed. The results show the proposed method can be applied within the relatively low frequency range (< 100 kHz), and has achieved good results.

Experiments are also conducted to validate the proposed method. For the wall-thinning defect with 1-mm depth and 40-mm axial length, the errors are found to be around 0.3 mm for depth and 25 mm for length predictions, which are satisfactory, showing its potential in real inspection. From the experiment, it has also been observed that the single excitation method is more efficient comparing with the multiple excitation method, and as the wave signal frequency increases, the prediction accuracy also improves. False predictions occurred in both excitation methods. Since the multiple excitation method obtains a wide frequency range SDI, the defect size can be narrowed based on other parameters such as the number of peaks of the SDI curve. Therefore, false predictions are easier to be avoided through multiple excitation method.

It should be noted that the corrosion defect in the present study has been simplified as wall thinning defect. Future research is expected to extend the proposed method to more realistic profiles of corrosion defects.

Data Availability Statement

All data, models, and code generated or used during the study appear in the submitted article.

Declaration of competing interest

The authors declare no conflicts of interest regarding the publication of this manuscript.

Acknowledgement

The authors gratefully acknowledge the support from Major Project of Fundamental Research on Frontier Leading Technology of Jiangsu Province (Grant No. BK20222006), the Jiangsu Province International Cooperation Project (BZ2022037), the Tencent Foundation through the XPLORER program, and the program of China Scholarships Council (202106090258).

References

Alleyne, D. N., T. Vogt, and P. Cawley. 2009. "The choice of torsional or longitudinal excitation in guided wave pipe inspection." *Insight-Non-Destructive Test. Cond. Monit.*, 51 (7): 373–377. The British Institute of Non-Destructive Testing.

Balogun, O., and J. D. Achenbach. 2020. "Application of the reciprocity theorem to scattering of surface waves by an inclined subsurface crack." *Int. J. Solids Struct.*, 207: 82–88. Elsevier.

Carandente, R., and P. Cawley. 2012. “The effect of complex defect profiles on the reflection of the fundamental torsional mode in pipes.” *NDT E Int.*, 46 (1): 41–47. Elsevier. https://doi.org/10.1016/j.ndteint.2011.11.003.

Catton, P., P. Mudge, and W. Balachandran. 2008. “Advances in defect characterisation using long-range ultrasonic testing of pipes.” *Insight-Non-Destructive Test. Cond. Monit.*, 50 (9): 480–484. The British Institute of Non-Destructive Testing.

Chua, C. A., P. Cawley, and P. B. Nagy. 2019. “Scattering of the fundamental shear guided wave from a surface-breaking crack in plate-like structures.” *IEEE Trans. Ultrason. Ferroelectr. Freq. Control*, 66 (12): 1887–1897. IEEE.

Croxford, A. J., P. D. Wilcox, B. W. Drinkwater, and G. Konstantinidis. 2007. “Strategies for guided-wave structural health monitoring.” *Proc. R. Soc. A Math. Phys. Eng. Sci.*, 463 (2087): 2961–2981. The Royal Society London.

Demma, A., P. Cawley, M. Lowe, A. G. Roosenbrand, and B. Pavlakovic. 2004. “The reflection of guided waves from notches in pipes: A guide for interpreting corrosion measurements.” *NDT E Int.*, 37 (3): 167–180. https://doi.org/10.1016/j.ndteint.2003.09.004.

Ditri, J. J. 1994. “Utilization of guided elastic waves for the characterization of circumferential cracks in hollow cylinders.” *J. Acoust. Soc. Am.*, 96 (6): 3769–3775. Acoustical Society of America.

Duan, W., and R. Kirby. 2015. “A numerical model for the scattering of elastic waves from a non-axisymmetric defect in a pipe.” *Finite Elem. Anal. Des.*, 100: 28–40. Elsevier.

Gao, T., Z. Yuanzhou, B. Ji, and Z. Xie. 2024. “Vision-based fatigue crack automatic perception and geometric updating of finite element model for welded joint in steel structures.” *Comput. Civ. Infrastruct. Eng.*, n/a (n/a). John Wiley & Sons, Ltd. https://doi.org/https://doi.org/10.1111/mice.13166.

Kubrusly, A. C., and S. Dixon. 2021. “Application of the reciprocity principle to evaluation of mode-converted scattered shear horizontal (SH) wavefields in tapered thinning plates.” *Ultrasonics*, 117: 106544. Elsevier.

Lee, J., J. D. Achenbach, and Y. Cho. 2018. “Use of the reciprocity theorem for a closed form solution of scattering of the lowest axially symmetric torsional wave mode by a defect in a pipe.” *Ultrasonics*, 84: 45–52. Elsevier.

Liu, X., J. Li, J. Zhu, Y. Wang, and X. Qing. 2021. “Cure monitoring and damage identification of CFRP using embedded piezoelectric sensors network.” *Ultrasonics*, 115: 106470. Elsevier.

Liu, X., B. Sun, Z.-D. Xu, X. Liu, and D. Xu. 2023. “A Data-Driven Danger Zone Estimation Method Based on Bayesian Inference for Utility Tunnel Fires and Experimental Verification.” *J. Perform. Constr. Facil.*, 37 (1): 4022078. American Society of Civil Engineers.

Løvstad, A., and P. Cawley. 2011. “The reflection of the fundamental torsional mode from multiple small defects in pipes.” *AIP Conf. Proc.*, 1335: 129–136. https://doi.org/10.1063/1.3591848.

Lu, H., Z.-D. Xu, T. Iseley, H. Peng, and L. Fu. 2023. *Pipeline inspection and health monitoring technology: The key to integrity management*. Springer.

Marzani, A. 2008. “Time–transient response for ultrasonic guided waves propagating in damped cylinders.” *Int. J. Solids Struct.*, 45 (25–26): 6347–6368. Elsevier.

Mei, H., and V. Giurgiutiu. 2019. “Guided wave excitation and propagation in damped composite plates.” *Struct. Heal. Monit.*, 18 (3): 690–714. SAGE Publications Sage UK: London, England.

Mitra, M., and S. Gopalakrishnan. 2016. “Guided wave based structural health monitoring: A review.” *Smart Mater. Struct.*, 25 (5): 0. IOP Publishing. https://doi.org/10.1088/0964-1726/25/5/053001.

Niu, X., W. Duan, H.-P. Chen, and H. R. Marques. 2019. “Excitation and propagation of torsional T (0, 1) mode for guided wave testing of pipeline integrity.” *Measurement*, 131: 341–348. Elsevier.

Pau, A., D. V Achillopoulou, and F. Vestroni. 2016. “Scattering of guided shear waves in plates with discontinuities.” *NDT E Int.*, 84: 67–75. Elsevier.

Pau, A., D. Capecchi, and F. Vestroni. 2015. “Reciprocity principle for scattered fields from discontinuities in waveguides.” *Ultrasonics*, 55: 85–91. Elsevier.

Peng, H., H. Lu, Z.-D. Xu, Y. Wang, and Z. Zhang. 2023. “Predicting solid-particle erosion rate of pipelines using support vector machine with improved sparrow search algorithm.” *J. Pipeline Syst. Eng. Pract.*, 14 (2): 4022077. American Society of Civil Engineers.

Phan, H., Y. Cho, and J. D. Achenbach. 2013. “Application of the reciprocity theorem to scattering of surface waves by a cavity.” *Int. J. Solids Struct.*, 50 (24): 4080–4088. Elsevier.

Rose, J. L. 2014. *Ultrasonic guided waves in solid media*. *Ultrason. Guid. Waves Solid Media*.

Shan, S., Y. Pan, and S. Xiao. 2022. “An efficient damage quantification method for cylindrical structures enhanced by a dry-point-contact torsional-wave transducer.” *Appl. Sci.*, 12 (2): 572. MDPI.

Tse, P. W., and X. Wang. 2013. “Characterization of pipeline defect in guided-waves based inspection through matching pursuit with the optimized dictionary.” *NDT E Int.*, 54: 171–182. Elsevier. https://doi.org/10.1016/j.ndteint.2012.10.003.

Wang, X., W. T. Peter, and A. Dordjevich. 2010. “Evaluation of pipeline defect’s characteristic axial length via model-based parameter estimation in ultrasonic guided wave-based inspection.” *Meas. Sci. Technol.*, 22 (2): 25701. IOP Publishing.

Wang, Z., C. Fang, K. Wang, and Z. Wu. 2023. “Guided wave propagation along surface of vertical solid partially submerged in horizontal liquid layer.” *Ultrasonics*, 129: 106893. Elsevier.

Wang, Z., S. Huang, S. Wang, Q. Wang, and W. Zhao. 2019. "Multifrequency identification and exploitation in Lamb wave inspection." *IEEE Access*, 7: 150435–150443. IEEE.

Xu, L., Y. Su, J. Yang, and Z. Su. 2023. "Frequency-dependent scattering of wideband laser-generated Rayleigh waves for vertical surface crack characterization." *Smart Mater. Struct.*, 32 (4): 45001. IOP Publishing.

Xu, Y., M. Luo, Q. Liu, G. Du, and G. Song. 2019. "PZT transducer array enabled pipeline defect locating based on time-reversal method and matching pursuit de-noising." *Smart Mater. Struct.*, 28 (7): 75019. IOP Publishing. https://doi.org/10.1088/1361-665X/ab1cc9.

Xu, Z.-D., C. Zhu, and L.-W. Shao. 2021. "Damage identification of pipeline based on ultrasonic guided wave and wavelet denoising." *J. Pipeline Syst. Eng. Pract.*, 12 (4): 4021051. American Society of Civil Engineers.

Zang, X., Z.-D. Xu, H. Lu, C. Zhu, and Z. Zhang. 2023. "Ultrasonic guided wave techniques and applications in pipeline defect detection: A review." *Int. J. Press. Vessel. Pip.*, 105033. Elsevier.

Zhang, J., X. Niu, A. J. Croxford, and B. W. Drinkwater. 2022. "Strategies for guided acoustic wave inspection using mobile robots." *Proc. R. Soc. A*, 478 (2259): 20210762. The Royal Society.

Zhang, J., X. Niu, A. J. Croxford, and B. W. Drinkwater. 2023. "Pipe inspection using guided acoustic wave sensors integrated with mobile robots." *NDT E Int.*, 139: 102929. Elsevier.

Zhu, C., Z.-D. Xu, H. Lu, and Y. Lu. 2022. "Evaluation of cross-sectional deformation in pipes using reflection of fundamental guided-waves." *J. Eng. Mech.*, 148 (5): 4022016. American Society of Civil Engineers.

Table 1. FE results for the axial length and depth of defect

	Actual	50 kHz	100 kHz	150kHz	50-150 kHz
Axial length (mm)	30	30.6 (30.6)	29.1 (30.6)	18.6 (30.7)	31.8 (30.3)
Depth (mm)	1	0.98 (0.96)	0.65 (1.02)	0.99 (1.01)	0.63 (1.11)

The results without considering attenuation are shown in parentheses.

Table 2. Experimental results for the axial length of defect.

	Actual	50 kHz	100 kHz	150kHz	50-150 kHz
Axial length (mm)	40	42.6	42.9	49.1	42.5
Percentage error (%)	\	6.5	7.25	22.75	6.25

Table 3. Experimental results for the depth of defect.

	Actual	50 kHz	100 kHz	150kHz	50-150 kHz
Depth (mm)	1	1.40	0.71	1.22	1.35
Percentage error (%)	\	40	-29	22	35

Table Caption List

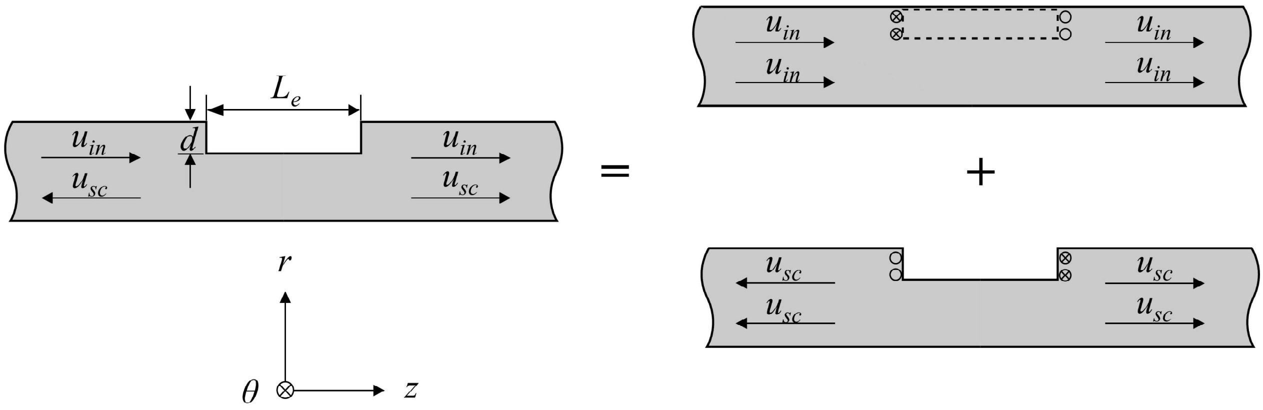

Fig. 1. Schematic of wave superposition principle.

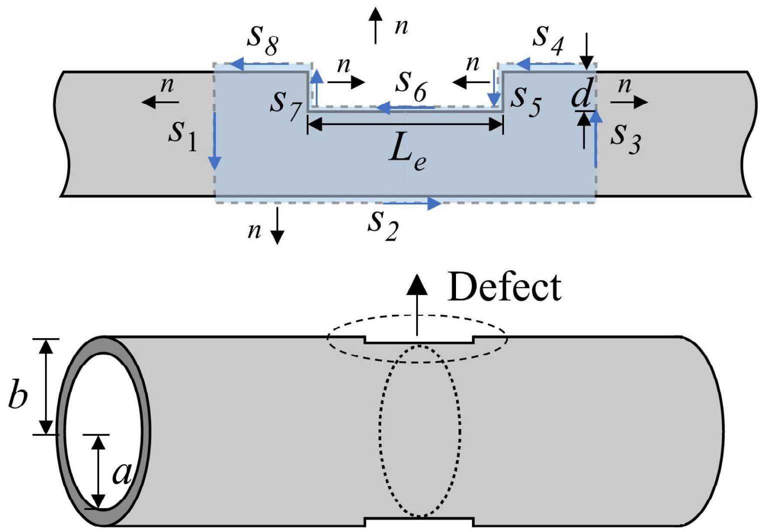

Fig. 2. Defect geometry and integration paths.

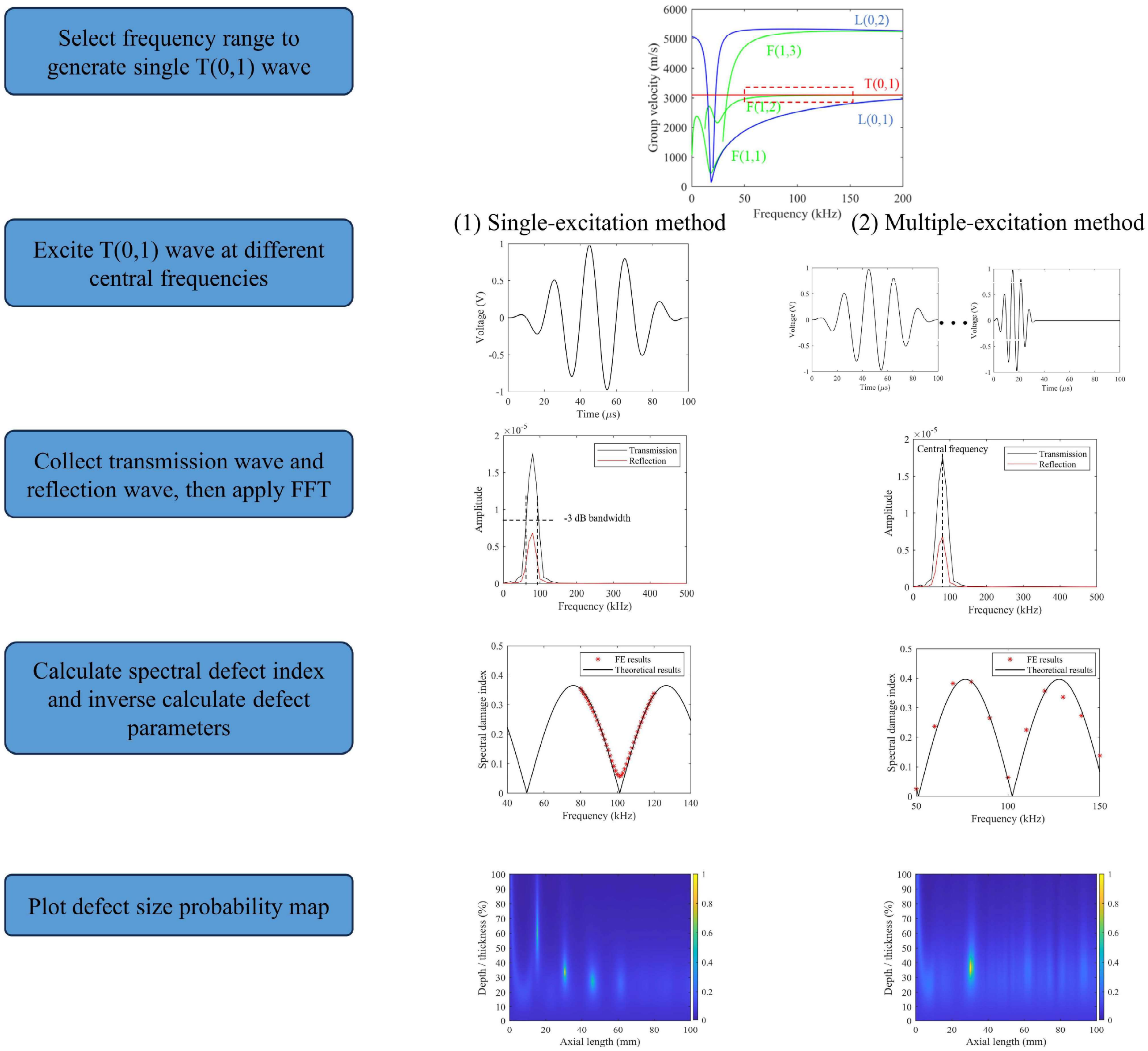

Fig. 3. Scheme of multi-frequency identification method.

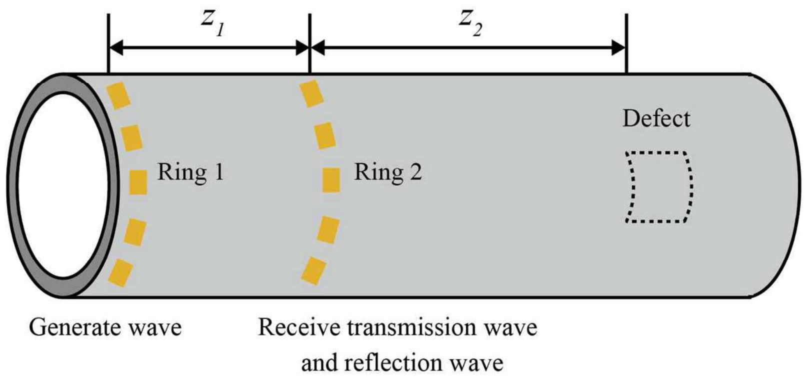

Fig. 4. Measurement configuration for multi-frequency identification method.

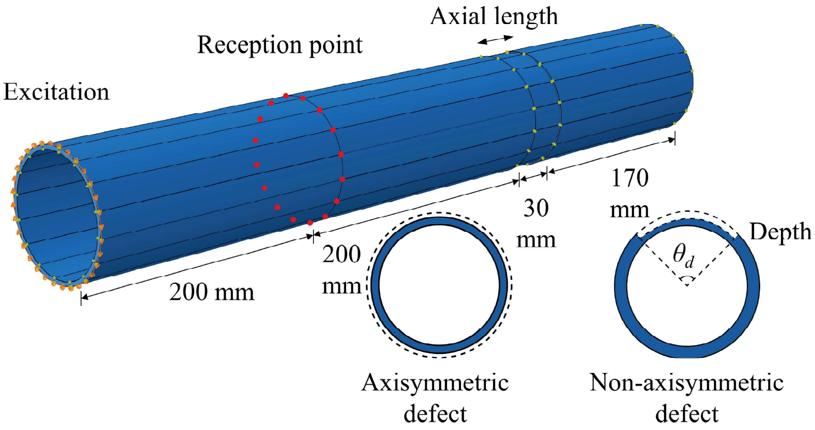

Fig. 5. Schematic of FE model.

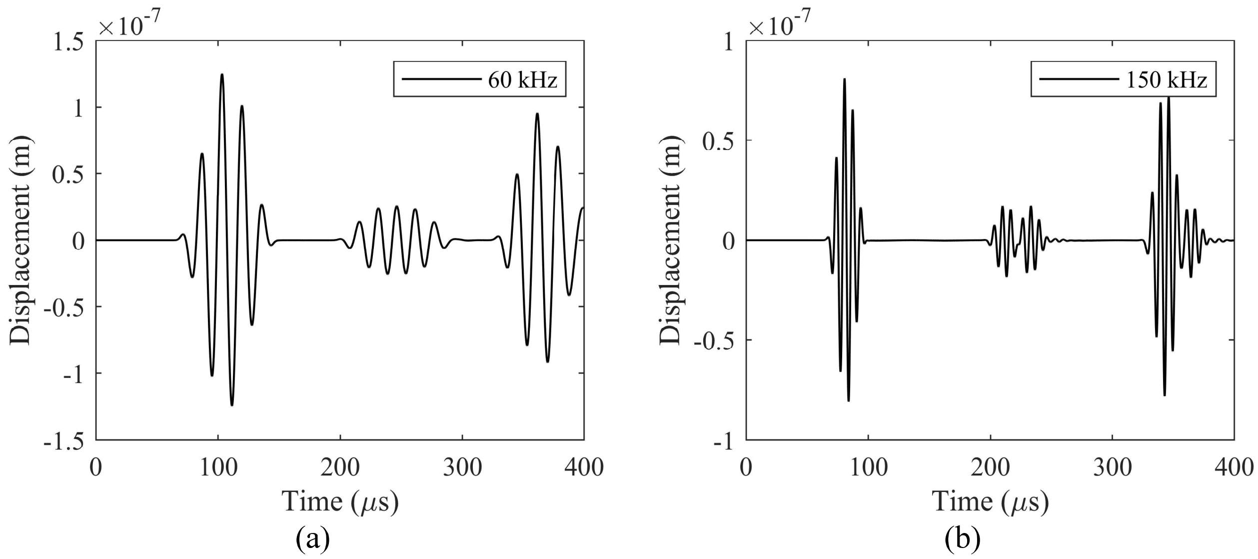

Fig. 6. FE results of received time domain signal for (a) 60 kHz excitation, (b) 150 kHz excitation.

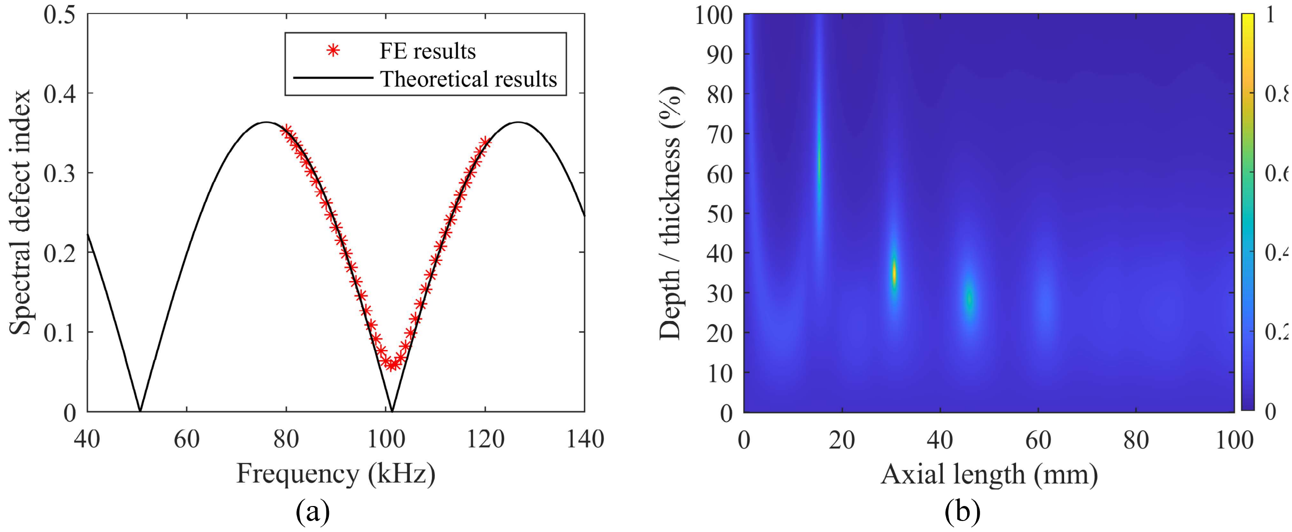

Fig. 7. FE results of (a) Spectral defect index for 100 kHz single-excitation method, (b) Defect probability map for 100 kHz single-excitation method.

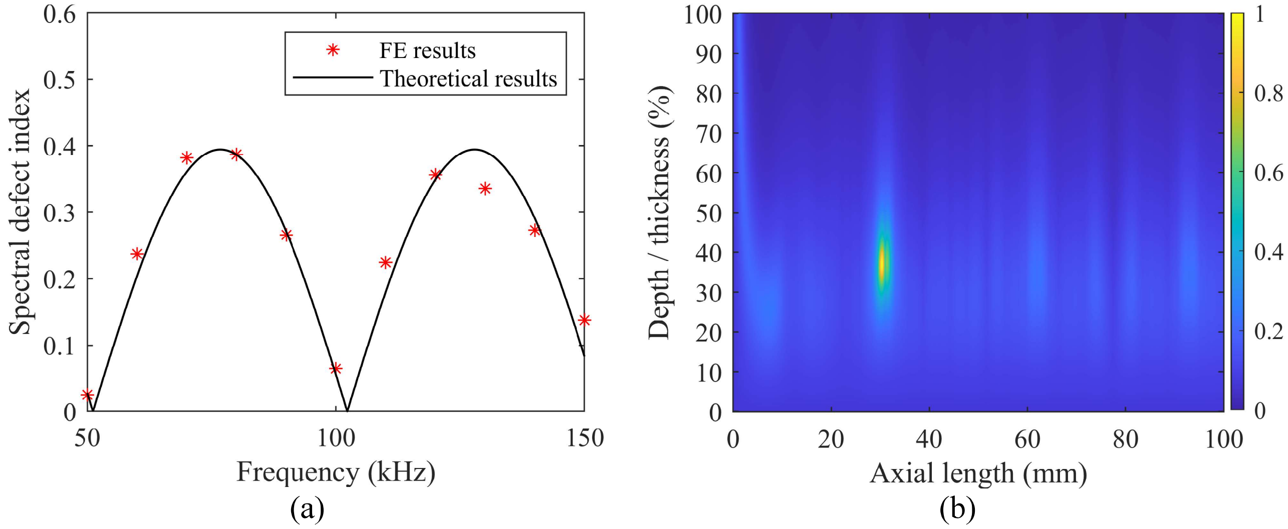

Fig. 8. FE results of (a) Spectral defect index for multiple-excitation method at 50-150 kHz, (b) Defect probability map for multiple-excitation method at 50-150 kHz.

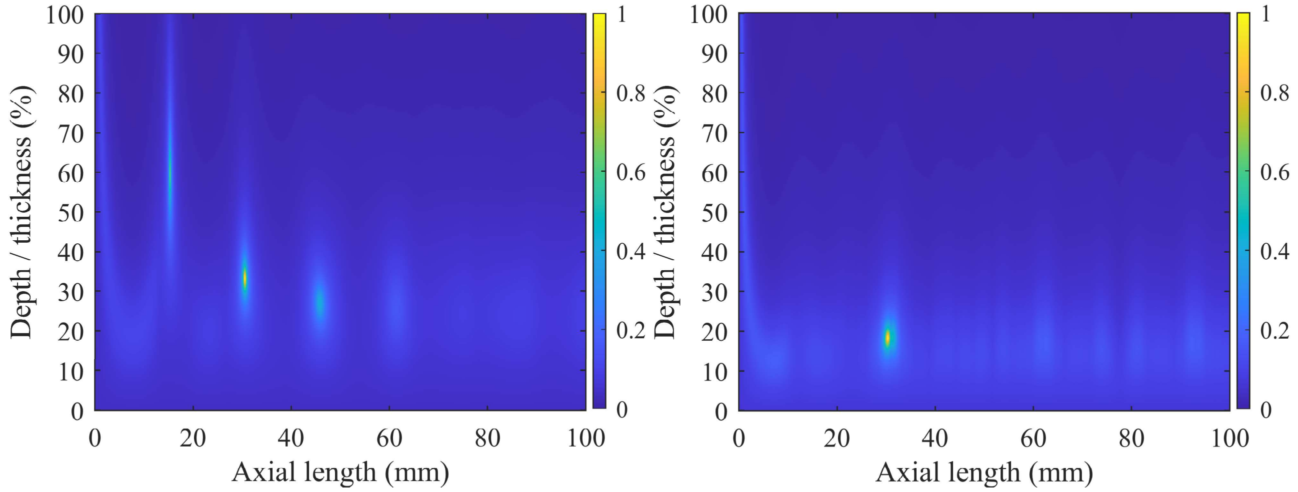

Fig. 9. (a) Defect size probability map for multiple-excitation method at 50-150 kHz, (b) Non-axisymmetric defect size probability map for multiple-excitation method at 50-150 kHz.

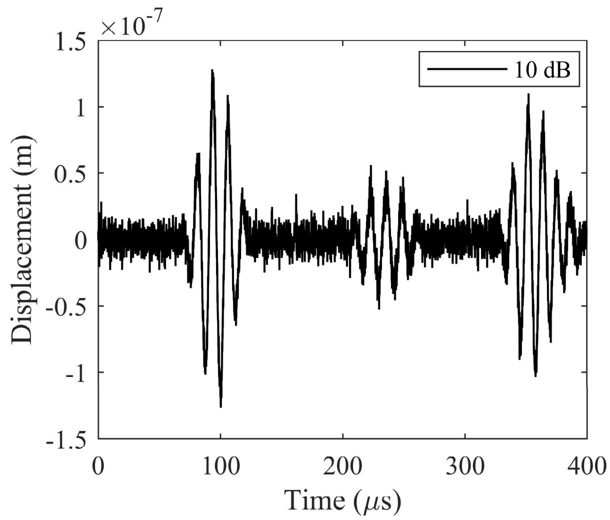

(a)

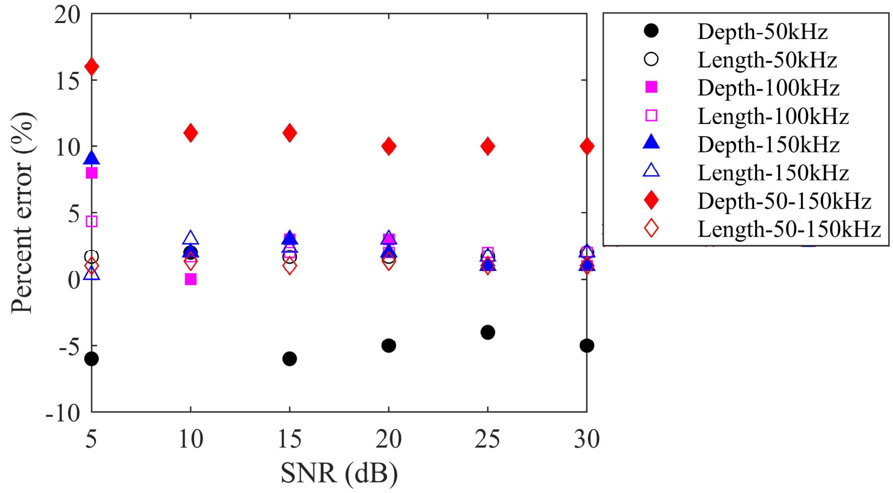

(b)

Fig. 10. Robustness test results. (a) Received signal with Gaussian white noise, SNR =10 dB, (b) Percentage error for FE results.

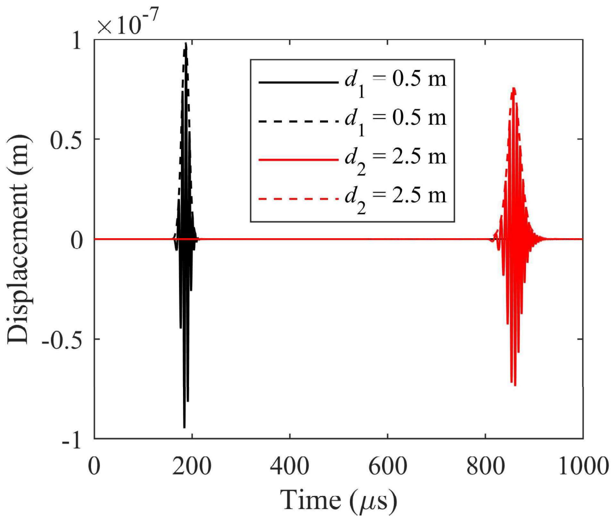

Fig. 11. FE results of received time domain signals and corresponding Hilbert envelopes for 140 kHz excitation

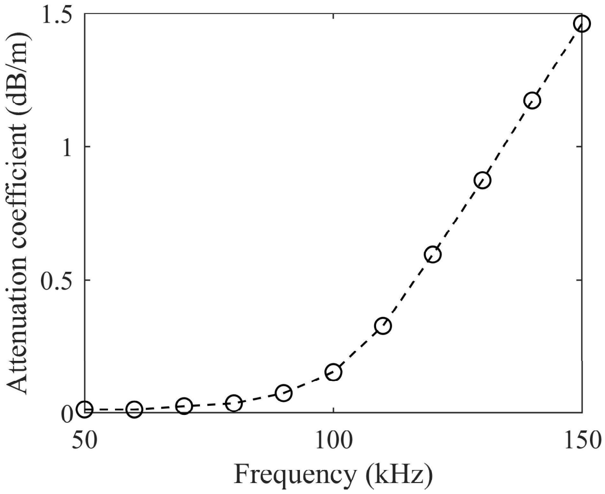

Fig. 12. T(0,1) wave attenuation coefficients calculated by FE model

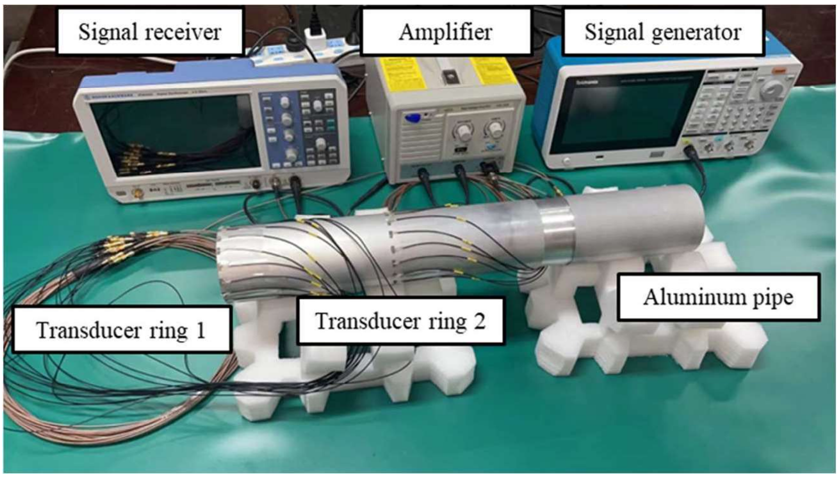

Fig. 13. A photo of experimental setup.

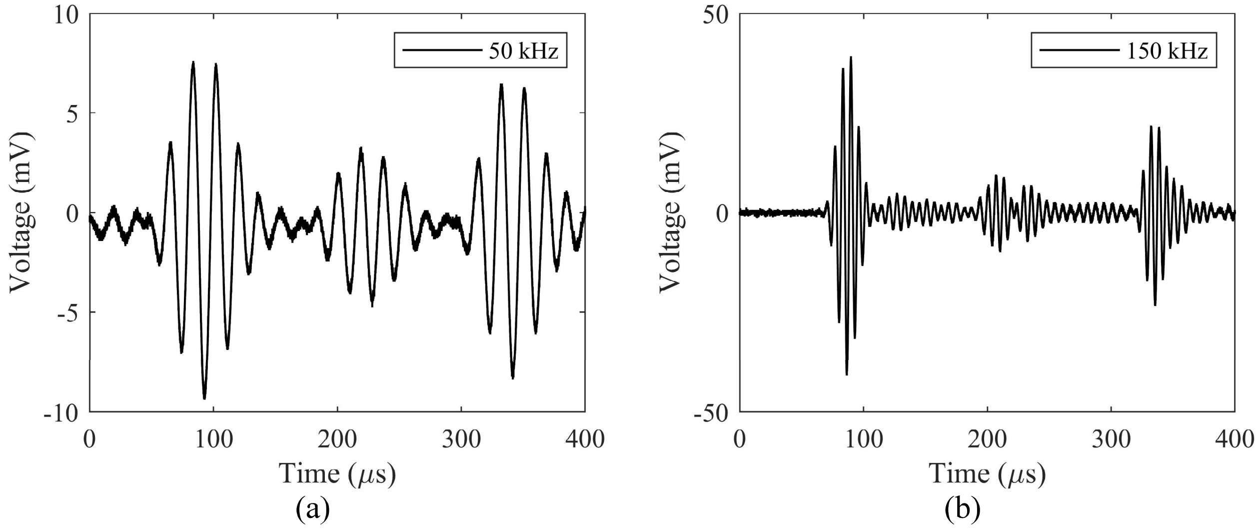

1

2 **Fig. 14.** Experimentally measured wave signals (a) at 50 kHz central frequency, (b) at 150 kHz central frequency.

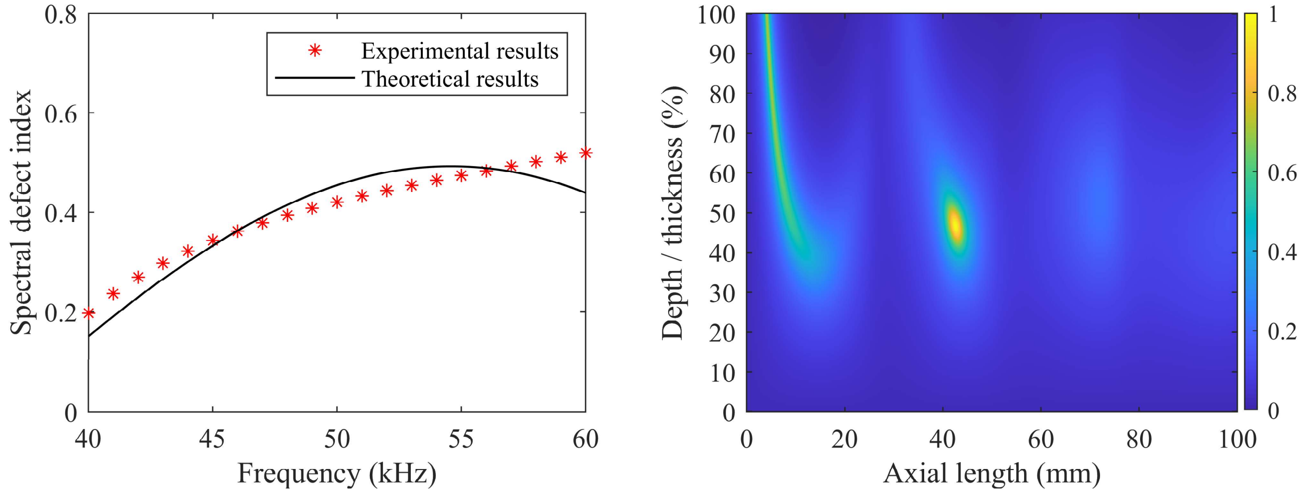

(a) (b)

Fig. 15. (a) Spectrum defect index of experimental results and theoretical results of single-excitation method at 50 kHz center frequency, (b) Defect size probability map for single-excitation method at 50 kHz center frequency.

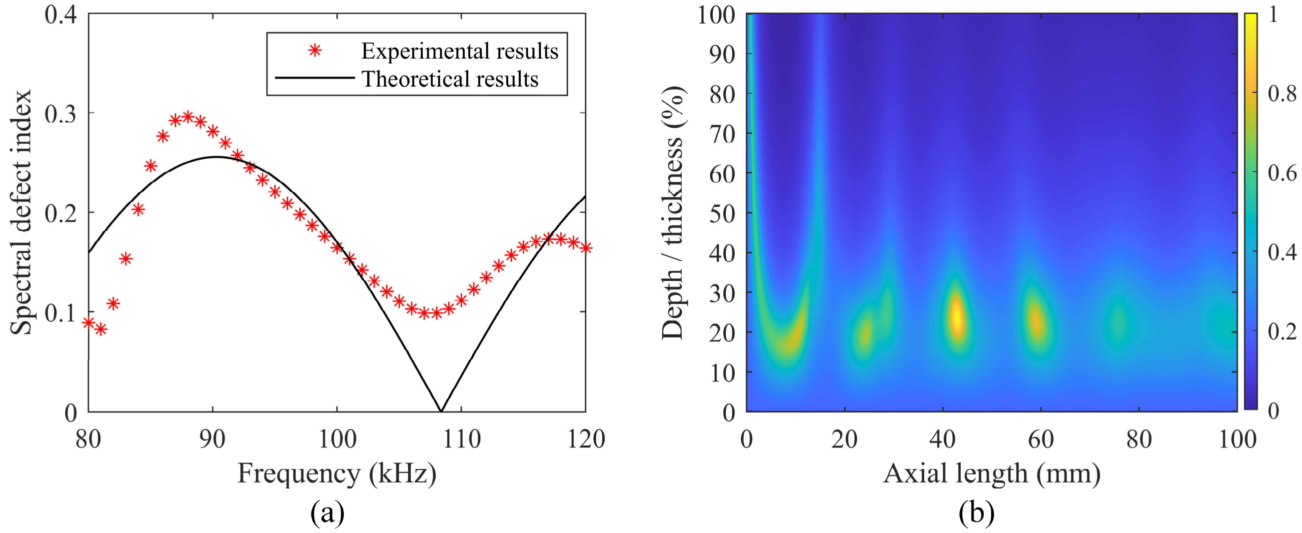

Fig. 16. (a) Spectrum defect index of experimental results and theoretical results of single-excitation method at 100 kHz center frequency, (b) Defect size probability map for single-excitation method at 100 kHz center frequency.

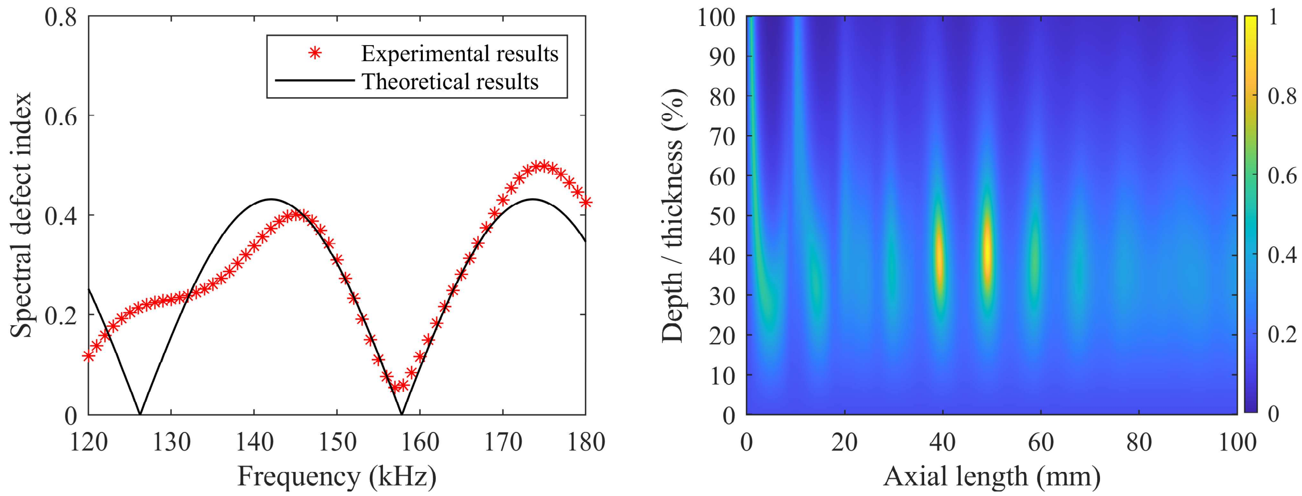

(a) (b)

Fig. 17. (a) Spectrum defect index of experimental results and theoretical results of single-excitation method at 150 kHz center frequency, (b) Defect size probability map for single-excitation method at 150 kHz center frequency.

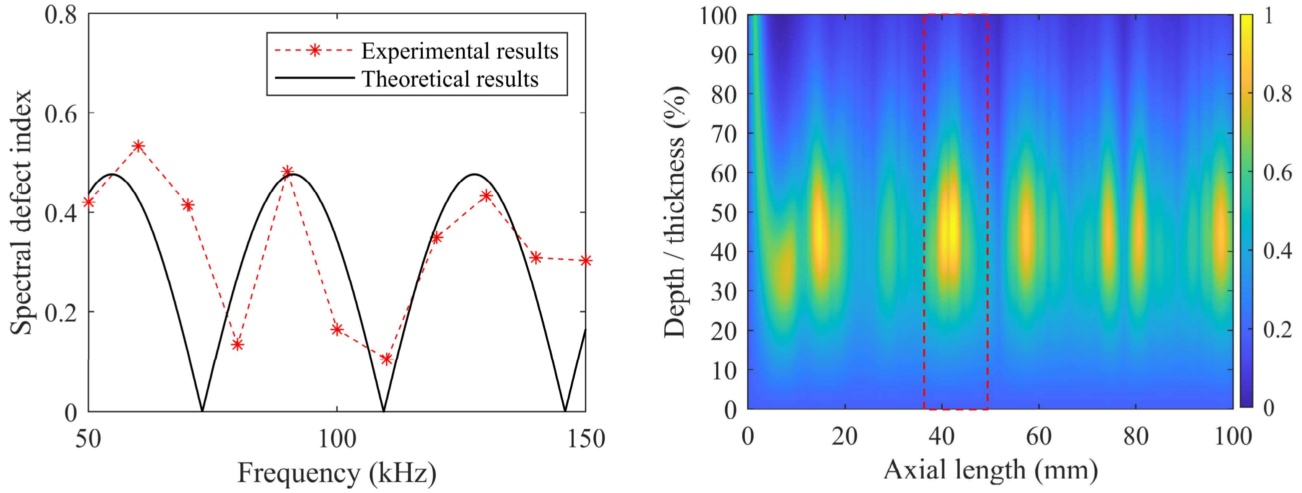

(a) (b)

Fig. 18. (a) Spectrum defect index of experimental results and theoretical results of multiple-excitation method at 50-150 kHz frequency range, (b) Defect size probability map for multiple-excitation method at 50-150 kHz frequency range.

Figure Caption List

Fig. 1. Schematic of wave superposition principle

Fig. 2. Defect geometry and integration paths

Fig. 3. Scheme of multi-frequency identification method

Fig. 4. Measurement configuration for multi-frequency identification method

Fig. 5. Schematic of FE model

Fig. 6. FE results of received time domain signal for (a) 60 kHz excitation, (b) 150 kHz excitation.

Fig. 7. FE results of (a) Spectral defect index for 100 kHz single-excitation method, (b) Defect size probability map for 100 kHz single-excitation method.

Fig. 8. FE results of (a) Spectral defect index for multiple-excitation method at 50-150 kHz, (b) Defect size probability map for multiple-excitation method at 50-150 kHz.

Fig. 9. (a) Defect size probability map for multiple-excitation method at 50-150 kHz, (b) Non-axisymmetric Defect size probability map for multiple-excitation method at 50-150 kHz.

Fig. 10. Robustness test results. (a) Received signal with Gaussian white noise, SNR=10 dB, (b) Percentage error for FE results.

Fig. 11. FE results of received time domain signals and corresponding Hilbert envelopes for 140 kHz excitation

Fig. 12. T(0,1) wave attenuation coefficients calculated by FE model

Fig. 13. A photo of experimental setup.

Fig. 14. Experimentally measured wave signals (a) at 50 kHz central frequency, (b) at 150 kHz central frequency.